Modelling the gradual through thickness porosity formation and swelling during the thermal aggression of thermoplastic based laminates

David Philippe, Benoît Vieille, Fabrice Barbe

Modelling the gradual through thickness porosity formation and swelling during the thermal aggression of thermoplastic based laminates

D. Philippe[a], B. Vieille[a,*], F. Barbe[a]

[a]*Groupe de Physique des Matériaux, CNRS, Normandie Univ., Univ. Rouen, INSA Rouen, 76000 Rouen, France*

Abstract

Impacting thermoplastic-based laminates by a high thermal energy -e.g. a flame- essentially causes the progressive deterioration of the matrix, involving solid-state transformations and dramatic variations of the thermomechanical properties. Throughout this process and because it is associated with significant through thickness gradients, the laminates retains a substantial capacity to sustain a mechanical load, even after matrix has melted. For temperatures higher than the melting temperature, the dominant mechanism of the matrix thermal decomposition is the formation of voids. Whereas they constitute a weakness from the mechanical point of view, they act as thermal insulators and contribute to the protection of the matrix on the side opposite to thermal aggression. Thus, describing accurately the kinetics of their formation is the key to a reliable control of the laminates thermomechanical properties evolution under fire conditions. As a prerequisite to this objective, the formation process was experimentally investigated. Results have evidenced the strong dependence of the porosity content and of the related swelling phenomenon to the time and temperature of thermal exposure. A mesoscopic Finite Element model representing porosities at a structural level was developed based on these observations. The porosity nucleation and the induced swelling were reproduced using a probabilistic approach to drive the progressive transformation of elements into porosities according to their thermal state.

Keywords: Thermal decomposition, Porosity, Thermoplastic resin, Numerical Analysis

*Corresponding author

Nomenclature

Variables and functions			
T	Temperature	t	Time
N	Number of finite elements	p	Nucleation probability
G	Nucleation rate	RE	Relative error
P_{int}	Internal pressure		
Parameters			
η	Volume fraction	m	Mass
ρ	Volumetric density	α	Pyrolysis degree
m	Mass	f_a	Adaptation function
Subscripts			
m	Matrix	f	Fiber
p	Porosity	cl	Composite laminates
w	Water	a	Air
Superscripts			
ref	Reference	ini	Initial
d	Decomposed	w	Water
a	Air		

1. Introduction

Under critical service conditions, aeronautical structural parts consisting of polymer matrix composite materials may be exposed to intense sources of thermal energy leading to high thermal gradients. The encountered temperature ranges from the ambient to the temperature of the thermal decomposition onset of the polymer (≈ 450°C [1]) and above. The capacity of the composite to sustain a thermomechanical load then depends on the degradation of the composite constituent properties, first and foremost those of the polymer matrix especially when it comes to high temperature conditions. The analyses of the interactions between mechanics and thermal transfers taking place under such conditions rely on very specific experimental means. Indeed, it is necessary to reproduce these critical operating conditions (e.g. fire) of composite materials intended for applications in aircraft engine. To this end, an approach based on both experimental and numerical analyses enables both a better understanding of the involved physics, and the development of a model to predict the progressive degradation of the state of the material. In the continuation of previous works [2, 3], this study focuses on the thermomechanical behaviour of a carbon fiber / polyphenylene sulphide thermoplastic [4, 5, 6] matrix laminates (C/PPS) [7]. As exposed to a heat source, the temperature of the laminates gradually increases which induces various phenomena. Whereas the carbon fibers can be considered unaltered up to temperatures of 700°C [8], the consequences on the matrix are numerous: thermal degradation, viscosity, damage, pyrolysis, delamination, oxidation, ...[9, 10]. These consequences are closely related to material state transitions of the polymer matrix at different temperatures: the glassy transition temperature ($T_g \sim 90°C$, from a semi-crystalline to a fully amorphous polymer), the melting temperature ($T_m \sim 280°C$, solid-liquid transition of the polymer), and finally the thermal decomposition temperature ($T_d \sim 450°C$ [1], from liquid to gaz and char or carbonated products). As a result, in the circumstances of a directional thermal aggression such as a flame, high thermal gradients develop and different solid state transformations occur over time from point to point of the laminates. Time and temperature dependencies of the properties thus need to be accurately accounted for in the process of describing and modelling the thermomechanical behavior of the laminates. As well, given the high contrasts of properties between fiber and polymer, this combination of a rapid heating with the heterogeneous nature of the composite meso-structure makes it necessary to adopt finely discretised time and temperature scales, both for the experimental and the numerical analyses.

In this context, this study deals with the description of the meso-structure changes in the laminates throughout the thermal decomposition process of the polymer matrix. Such an explicit decomposition representation is a pre-requisite to any investigation into the evolution of the thermomechanical behavior under the circumstances of a fire. As temperature increases and exceeds T_d, the pyrolysis of the matrix becomes a dominant mechanism. Thus, the polymer matrix, which is initially at liquid state undergoes a gradual

transformation into mainly pyrolysis gas and a carbon residue (named char, see [11] for the chemical composition). During the process, cavities form, filled with pyrolysis gas. It can be characterized according to its kinetics. Thermal decomposition of thermoplastic polymers has been widely covered experimentally in terms of mass loss according to time, temperature, heat rate, and atmosphere [12, 13, 1, 14, 15]. It was shown that different rate laws could be identified to reproduce the kinetics of mass loss [16, 17, 18, 2]. The progress of the thermal decomposition in terms of mass loss is generally characterized by a pyrolysis degree α which can be determined experimentally from the variations of the sample mass during the decomposition. Alternatively, α can be estimated from one of the theoretical laws based on the assumption that the pyrolysis progress rate is modelled by a multiplicative decomposition $f\,(T)\,.g(\alpha)$ depending on the temperature (Arrhenius-type) and the pyrolysis degree [16, 19, 20].
However, these studies do not consider the influence of the presence of cavities within the structure, although they drastically alter both the structural and the thermomechanical behavior of the laminates [2]. From a structural viewpoint, the cavities induce the presence of high-pressure gas pockets which, as they expand, introduce an increase in the volume of the macro-structure through peeling. This behaviour is even more amplified by the fact that there is less matrix to ensure the load transfer within the laminates [21]. As a consequence on the thermomechanical properties, the behaviour of the material is dramatically altered since solid matter is replaced by gas [22]. During fire exposure, time-dependent thermal gradient within the laminates will lead to a disparity of matrix states at the scale of a ply. Such local variations may be considered at a mesoscopic scale by means of an explicit representation of the matrix and fiber bundles arrangement. It is to be noted that on the lateral borders of the thermally exposed sample (faces where the laminates were cut), direct contact with oxygen occurs which can lead to the oxidation of both char and fibers in addition to the pyrolysis decomposition [23]. It will however not be considered throughout this paper since the focus was set at understanding the phenomena in the core of the material.
It was chosen to describe the reaction kinetics according to the porosity content within the laminates rather than in terms of mass loss. As in the Gurson Tvergaard Needleman (GTN) model [24], different constitutive models account for the volume fraction of porosities to describe damage in a solid material. However, these models consider the porosity content as a global variable, which is not compatible with the numerical model's ultimate usage of accounting for local thermal gradients combined with swelling. An explicit representation of the cavities inside the matrix of the laminates mesostructure was therefore privileged. Finite elements of the matrix are progressively turned into porosities to build up these cavities. Doing so, structural effects (such as swelling) and porosity-specified thermal transfers can be taken into account locally.
For this original proposal, the considered mechanism of porosity formation is their nucleation, as discussed in section 3.2. The kinetics model to describe this process has been developed on the basis of experimental observation: liquid-gas transition of the finite elements of matrix takes place according to a random process controlled by temperature and time; the parameters involved in the probabilistic law governing this random process have been identified from experimental analyses for different times and temperatures of thermal exposure.
The swelling mechanism is reproduced by applying an internal pressure within the porosities. Thermal exposure was in a first step chosen as homogeneous so that no thermal and decomposition gradient unnecessarily complicate the understanding of the phenomena. The heterogeneous case (representative of the fire exposure scenario, see Fig. 1) will be taken into consideration later on by using a small-scale kerosene burner [25, 26]. It is to be noted that this article focuses on the development of the thermal decomposition numerical model, and coupled thermomechanical loading will be the object of future works.

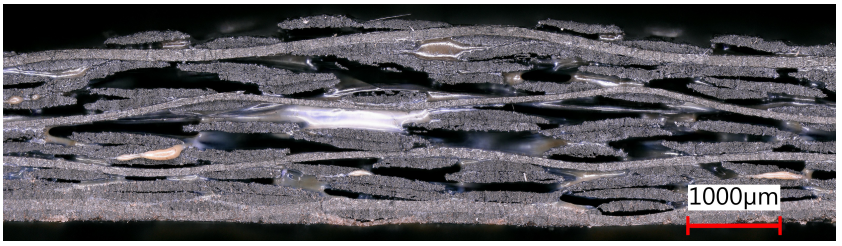

Figure 1: Decomposed C/PPS sample after 115kW/m^2 kerosene flame exposure for one minute

Following sections present: (i) the characterization of the kinetics according to temperature and time,

(ii) the way this kinetics is introduced into a meso-scale numerical model of the laminates and (iii) final discussion and experimental / numerical comparisons.

2. Experimental results

2.1. Materials and methods

This study deals with C/PPS laminates consolidated according to an industry-used stacking sequence, namely the quasi-isotropic (QI) (see Fig. 2 for stacking sequence overview). It is composed of seven layers alternating [0°/90°] plies and [±45°] ones.

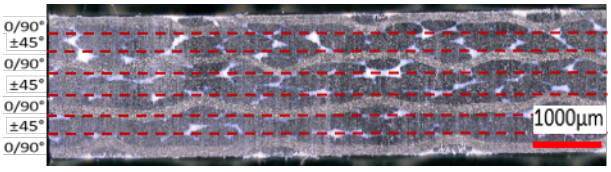

Figure 2: QI C/PPS stacking sequence

The experimental method used to determine the porosity content (a volume fraction) as well as the protocol followed are presented respectively in Appendix A and Appendix B.

2.2. Qualitative analyses on porosity formation

Qualitative considerations based on optical observations confirmed that porosity formation highly depends on time and temperature at various levels as can be seen on Fig. 3 for observations obtained in a central slice.

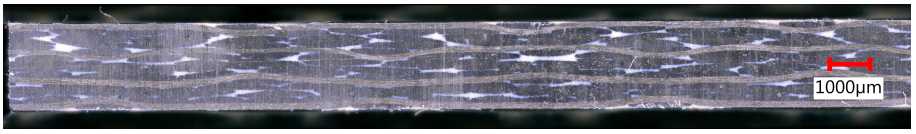

(a) Virgin sample

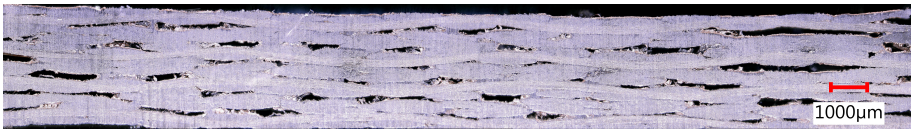

(b) 465°C – 7min – Porosity content: 28.6%

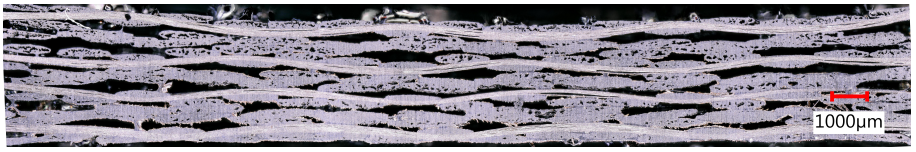

(c) 530°C – 7min – Porosity content: 43.2%

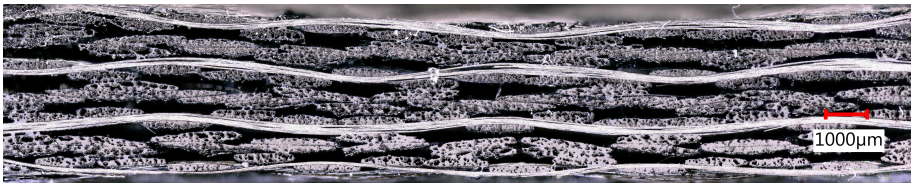

(d) 600°C – 5min – Porosity content: 54.8%

Figure 3: Optical microscope observations of thermally decomposed C/PPS laminates under homogeneous thermal exposure at different temperatures and instants

Overall, the porosities progressively replace the virgin matrix and tend to form pockets of localized pyrolysed areas. As they appear, porosities can be classified into two categories: (i) open porosities which are connected to the external environment either directly or by a network of voids created during the progressive

decomposition of the matrix within the laminates; the pyrolysis gases generated inside these porosities can then escape from the porosities; (ii) closed porosities which remain trapped within the material and are still filled with pyrolysis gases. Their influence on the geometrical changes of the laminates also vary. Whereas closed porosities tend to induce a homogeneous swelling of the material (due to internal pressure), open ones disrupt this homogeneity along the borders of the sample. Indeed, the escape of the gases is an abrupt process making the swelling far more important at the edges of the composite than in the middle, making it less thick in the center.
The process of porosity formation can be described by three consecutive mechanisms: (i) nucleation, mostly within matrix-rich areas, (ii) growth of these porosities and (iii) coalescence. Coalescence results in interconnected porosities over the whole length of the sample, therefore connecting them to free edges which releases the pyrolysis gas.
As temperature increases, the thermal decomposition state progresses. However it is not a linear evolution since at high temperatures (beginning at 530°C and clearly visible at 600°) new areas of porosities appear within the fiber bundles, resulting in a severe fiber bundles / matrix debonding. These intra-bundle porosities may result from three mechanisms: (i) the decomposition of the polymer matrix constituting the fiber bundle (volume fraction of 17%), (ii) the debonding of the fibers and (iii) oxidation of the fibers due to the air flux and the oxygen which is released as the polymer matrix decomposes into gas [27]. The onset of this phenomenon can be observed on Fig. 3 at 600°C. Besides, the time of exposure at a given temperature mainly contributes to continue the process of porosity formation already in place, without introducing new ones.
For a better understanding of the porosity distribution, X-Ray tomography observations are used to perform a 3D numerical reconstruction of the samples (Fig. 4). Afterwards, internal porosities can be extracted by setting a greyscale threshold. To set aside the edge effects, porosities are extracted from the center of the sample. It is observed in this particular example that the porosity distribution is rather homogeneous (each color distinguishing a separate porosity), which was expected for a homogeneous thermal exposure. However, this technique is more relevant in the case of a non uniform thermal exposure (e.g. one-face flame impact) since it is expected that the thermal gradients induce a significant porosity gradient through the thickness.

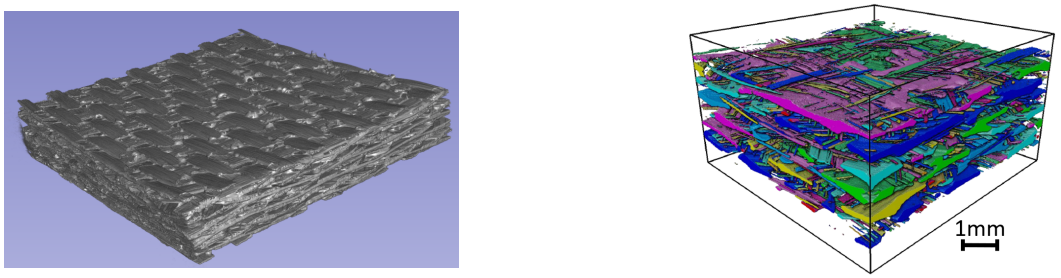

(a) (b)

Figure 4: 3D reconstruction from tomography slices obtained from C/PPS laminates - $25 \times 25\text{mm}^2$ - 530°C - 7min - Porosity content: 42%. (a) Whole sample, (b) extracted porosities. Colors correspond to porosity network

2.3. Quantitative analyses on porosity formation

As explained in subsection Appendix A, the porosity content was determined according to various times and temperatures. Although the initial matrix volume represents 50% of the initial volume of the laminates, porosity content goes over 50% since the final volume gets larger and since it can be reasonably assumed that the carbon fiber volume remains unchanged.
First, the sample size effect on the porosity content was investigated. As an example, Fig. 5 shows that, after a 530°C thermal exposure for 2min, only a small difference is obtained between the $25 \times 25\text{mm}^2$ samples and the converged values.

The time evolution of the porosity content $\eta_p\,(t, T)$ is depicted in Fig. 6 for temperatures of 465°C, 500°C, 530°C and 600°C for the laminates. Results show a similar trend of evolution for all considered conditions: a rapid increase during the first minutes and then a saturation to an asymptotic value depending on the temperature of treatment. However a major limitation for numerical modelling was observed at 7

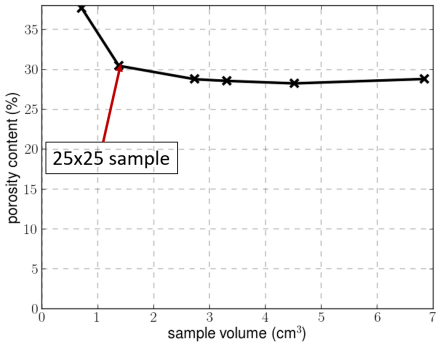

Figure 5: Evolution of the porosity content over sample volume after a 530°C thermal exposure for 2min

minutes. It was the direct consequence of the sudden thickness drop at 5 minutes for temperatures of 530° and higher (see Fig. 7(a) in which the final thickness is normalized by the initial one). As the temperature and time of exposure became too elevated, structural damage made the laminates unable to withstand such a swelling which resulted in a collapse of the material. The swelling appeared to be limited to a maximum factor of 1.7 of the initial thickness in every scenario, confirming the above-mentioned maximum expansion of the laminates before collapse. Since the porosity volume determination highly depends on the thickness, its collapse strongly decreases η_p. However the mass loss increase (Fig. 7(b)) compensates the thickness decrease in the porosity content calculation (Eq. A.1). As a result, the porosity content remains steady.

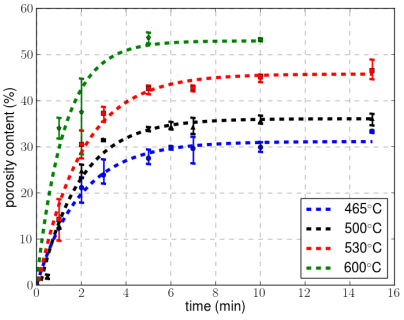

Figure 6: Evolution over time of porosity content for different temperatures of exposure, as measured with the geometry-based method

Considering that the mechanisms leading to the collapse of the laminates are not fully understood yet, it was chosen to limit the exposure time to 5 minutes in the numerical modelling for temperatures above 500°C.

3. Numerical modelling

3.1. Domain of computation

The large discrepancies between the matrix and the fiber bundles in terms of thermomechanical behavior and thermal decomposition process (Fig. 3) has led to consider a mesoscopic scale based on the previous work of Carpier et al. [21]. A three-dimensional mesoscopic numerical model of the composite was hence created (using the software TexGen [28]), representing explicitly matrix and yarns in 1/28th of a Representative Volume Element (RVE), i.e. a volume of $1.7 \times 1.03 \times 2.20\text{mm}^3$ (cf. Fig. 8 (a) and (b)). To start the analyses, the dimensions of study were set to get a fine discretization (5,000,000 elements), and the location of the subdomain was chosen to have the same volume fraction of matrix as in the laminates. The mesh refinement is depicted on Fig. 8 (c) with a zoom on the subdomain. Further analyses on sensitivity to mesh size are presented in section 3.2.5. The Finite Element calculations were performed using Z-Set [29]. The reader should refer to [21] for a deeper description of the laminates numerical representation, the meshing process as well as the various thermomechanical properties and boundary conditions considered.

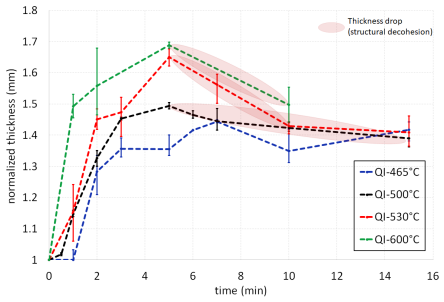

(a) Sample thickness

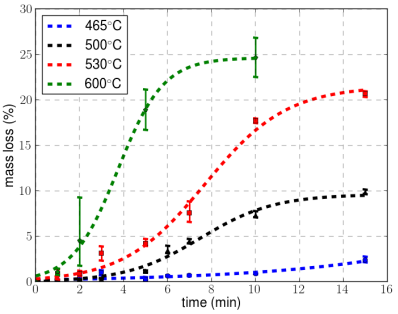

(b) Sample mass loss

Figure 7: Evolution over time of the geometry-based method characteristic quantities (thickness and mass) for different temperatures of exposure

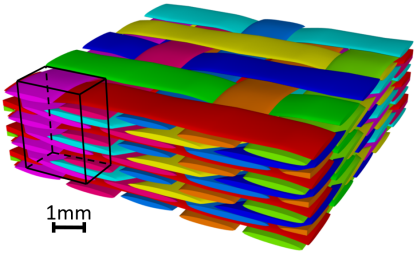

(a) RVE and selected subdomain

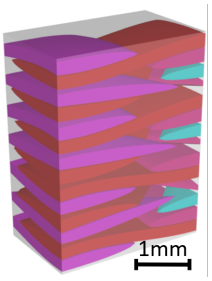

(b) QI 1/28th subdomain

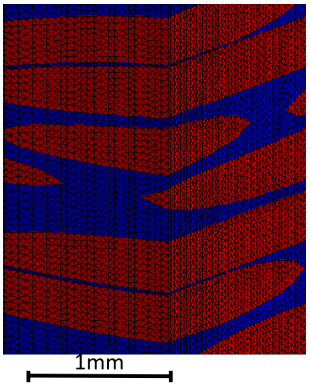

(c) Zoom on the subdomain mesh

Figure 8: 3D mesoscopic numerical model of the laminates. Colors are used to differentiate the fiber bundles

3.2. Nucleation of the porosities

At this stage of the modelling development - aimed to be developed further in future works - it was chosen to focus on the porosity nucleation mechanism out of the three possible mechanisms, viz. nucleation, growth and coalescence. Two main reasons motivated this choice: it is the first step of the porosity formation and a compromise between computation time and modelling complexity.

In the numerical model, the porosity nucleation and the swelling mechanisms at a given instant of the decomposition are introduced according to two successive steps: first the nucleation of porosities and then their swelling. In order to reproduce the nucleation of porosities, the numerical separation of the nucleation and swelling processes is performed by using an intermediate normalization of the experimental η_p according to the thickness of the samples. The normalized η_p^{ref}, noted η_p^*, then represents the porosity content in a sample which would have been brought back to its initial thickness before swelling.

The modelling applies to a subdomain of computation which is embedded within the laminates. No difference is made between closed porosities at the core and open porosities along the edges. With such a representation and since the volume fraction of matrix in the subdomain is equal to that of the laminates, the kinetics of porosity formation within the subdomain can be assumed to be representative of that of the laminates with large dimensions. As a corollary to these working hypotheses, the kinetics of porosity formation is solely characterized by the volume fraction of porosities inside the subdomain.

The nucleation was implemented as mesh elements of matrix progressively turning into gas based on a probabilistic law depending on time and temperature.

3.2.1. Probability based kinetics model

For sake of clarity at this stage of the presentation, the kinetics model is presented in the model configuration of a fixed temperature T (so that no dependence on T is mentioned yet; it is introduced in a second step) and of a mesh made up of matrix and porosity elements exclusively.

Let $N_m(t)$ and $N_p(t)$ denote the numbers of matrix elements and porosity elements at the instant t, within a set of $N_m^0 = N_m(t = 0)$ matrix elements at the initial instant. Owing to conservation, the following equality holds:

$$N_m(t) + N_p(t) = N_m^0 \qquad \forall t \geq 0 \tag{1}$$

Noting $\dot{N}_p(t)$ the rate of production of porosity elements at time t, the number of produced porosities within the time interval $[t, t + \Delta t]$ is

$$\Delta N_p(t) = \dot{N}_p(t)\,\Delta t \tag{2}$$

If each matrix element is assigned a probability p to transform into a porosity within $[t, t + \Delta t]$ and assuming that $N_m(t)$ is very large, the complete set of random draws over the $N_m(t)$ candidate elements leads to the following expected number of produced porosities:

$$\Delta N_p(t) = pN_m(t) \tag{3}$$

The combination of Eq. 2 and 3 enables to define p according to a function $G(t)$ -depending only on time- and to the time duration Δt:

$$\frac{p}{\Delta t} = G(t) \qquad \text{where} \quad G(t) = \frac{\dot{N}_p(t)}{N_m(t)} \tag{4}$$

Assuming that all the elements have the same volume, the rate of porosity content $\dot{\eta}_p(t)$ and the volume fraction $\eta_p(t)$ at an instant t can be expressed by:

$$\dot{\eta}_p(t) = \frac{\dot{N}_p(t)}{N_m^0} \qquad \eta_p(t) = \frac{N_p(t)}{N_m^0} \tag{5}$$

The combination of Eq. 1, 4 and 5 leads to the following partial differential equation, of which the volume fraction of porosity $\eta_p(t)$ is solution:

$$\dot{\eta}_p(t) = G(t)\left(1 - \eta_p(t)\right) \qquad \forall t \geq 0 \tag{6}$$

By repeating the reasoning from Eq. 1 to Eq. 7 for a different temperature, one obtains the following partial differential equation to describe the temperature-dependent kinetics model of porosity formation:

$$\begin{aligned} &\dot{\eta}_p(t,T) = G(t,T)\left(1 - \eta_p(t,T)\right) \qquad \forall t \geq 0,\ \forall T \geq T_{\mathrm{d}} \\ &\text{where} \quad G(t,T) = \frac{p(t,T,\Delta t)}{\Delta t} \end{aligned} \tag{7}$$

A similar approach is regularly used in theoretical physics to study the evolution of particle decay over time. It emanates from the theory of radioactive decay which was first developed by Rutherford and Soddy in 1902 [30]. The G factor is then a constant decay rate and an explicit expression of η_p can be obtained (proportional to $exp(-Gt)$).
From Eq. 7 it follows that, given a time discretisation in terms of Δt (not necessarily constant), the kinetics is completely described from the probability $p(t, T, \Delta t)$. There thus only remains to attribute an analytical form to $p(t, T, \Delta t)$ -or alternatively $G(t, T)$-, after which Eq. 7 can be numerically solved to approximate $\eta_p(t, T)$ under the assumption of a very large set of matrix elements. This is under concern in subsection 3.2.2.
In the particular case of a constant time increments Δt, a closed form of $\eta_p(t)$ can be obtained.
Let us note $t^{(k)} = k\Delta t$ the time at the k-th increment, $p^{(k)} = p\left(t^{(k)}\right)$ the corresponding probability, and $\eta_p^{(k)}$ the corresponding porosity content. After the definition of η_p and p, $\eta_p^{(k)}$ can be described by the following recursive sequence:

$$\begin{cases} \eta_p^{(0)} = 0 \\ \eta_p^{(k+1)} = \left(1 - p^{(k+1)}\right)\eta_p^{(k)} + p^{(k+1)} \end{cases} \tag{8}$$

As to illustrate with $t^{(3)} = 3\Delta t$: $\eta_p^{(3)} = p^{(1)} + p^{(2)} + p^{(3)} - p^{(1)}p^{(2)} + p^{(2)}p^{(3)} + p^{(1)}p^{(3)} + p^{(1)}p^{(2)}p^{(3)}$
Let $C_{i,k}$ denote the set of possible combinations of i elements out of k and let us note $c \in C_{i,k}$ any of these

combinations. From a recurrence analysis, it can be shown that the volume fraction at the time $t^{(k)}$ is:

$$\eta_p\left(k\Delta t\right) = \sum_{i=1}^{k} \left(-1\right)^{i+1} \sum_{c \in C_{i,k}} \prod_{j \in c} p^{(j)} \tag{9}$$

If, further, the probability $p^{(k)}$ is set constant over time increments, Eq. 9 is simplified into:

$$\eta_p\left(k\Delta t\right) = \sum_{i=1}^{k} \left(-1\right)^{i+1} \binom{k}{i} p^{(i)} \qquad \text{with} \quad \binom{k}{i} = \frac{k!}{i!\ (k-i)!} \tag{10}$$

As for $\eta_p(t,T)$ determined from Eq. 7, the assumption pertaining to the closed form of Eq. 10 is that the number of matrix elements is very large. This closed form has been retained as the reference asymptotic kinetics law, noted $\eta_p^{\infty}(t,T)$, for the analyses of the effect of domain size and mesh refinement in subsection 3.2.5.

3.2.2. Probabilistic law

According to Eq. 7, if the expression of $G(t,T)$ (or alternatively $p(t,T,\Delta t)$) is prescribed, then the temperature dependent evolution of the porosity content can be described completely. One way to build up $G(t,T)$ would be to derive it from the classical partial differential equation describing pyrolysis kinetics (cf. [31]). This equation gives the rate of the degree of thermal decomposition $\dot{\alpha}(t,T)$ according to a temperature dependent rate factor in the form of an Arrhenius function and to a reaction model depending on α. As detailed in [3], the identification of the decomposition kinetics of the polymer matrix can be made from different approaches, more or less consistent with the involved physics, and all of them are based on thermogravimetric analyses of the polymer matrix.

In the present work it is purposely chosen to develop a model from macroscale measurements of thermally-induced mass and dimensions evolutions. Along with this choice, the main role assigned to $G(t,T)$ is to enable the reproduction of a macroscale phenomenology from a microscale mechanism -porosity nucleation- on a wide range of temperatures. Given the extant of scales and the spectrum of thermomechanical properties to deal with in this model, a pragmatic choice is made for the construction of $G(t,T)$: it can be a phenomenological function calling on as few parameters as possible and necessarily positive.

According to experimental results at each considered temperature T, the rate of porosity content $\dot{\eta}_p(t,T)$ is maximal at $t=0$ and monotonously decreases over time until $\eta_p(t,T)$ reaches a saturation value. This evolution corresponds to a probability of nucleation which itself should be maximal at $t=0$ and then would continuously decrease to zero over time. The form of $G(t,T)$ proposed in Eq. 11 enables to reproduce this trend:

$$G\left(t,T\right) = \frac{A\left(T\right)}{t+B} \tag{11}$$

$A(T)$ depends on the temperature while B correspond to a constant (positive) characteristic time. $A\left(T\right)$ should describe the dependence to T, potentially non linear, using as few parameters as possible. In order to adapt the conditions for an efficient identification of these parameters, a first round of analyses was performed at a reference temperature T^{ref} in the medium range of considered temperatures ($T^{ref} \in [T_d, 600°\mathrm{C}]$), at which a comprehensive set of mechanisms is involved in the phenomenon of decomposition. This preliminary functional analysis has led to the expression of $G\left(t,T\right)$ provided in Eq. 12. The parameters and their respective roles are reported in Table 1. The provided values result from the identification which is explained in subsection 3.2.3.

$$G\left(t,T\right) = \frac{a_1 + a_2\left(\dfrac{T-T_d}{T^{ref}-T_d}\right)^b}{t+\tau} \tag{12}$$

Parameter	Unit	Value	Main role
a_1	No unit	0.205	Affects G for $T = T_d$
a_2	No unit	0.139	Dependence of G to T
τ	Time (s)	15	Time shift at the initial time
b	No unit	1.15	Dependence of $\frac{\partial G}{\partial T}$ to T
T^{ref}	°C	530	Reference temperature

Table 1: Parameters used to define $G\left(t,T\right)$ as given by Eq. 12

3.2.3. Identification of $G(t,T)$

The identification of the parameters of $G\left(t,T\right)$ is performed by optimisation. It is a classical iterative process where, given a set of parameters $P = \{a_1, a_2, \tau, n\}$, the following operations are performed at each step:

- the partial differential equation Eq. 7 is numerically solved (Euler scheme based on a small Δt)
- its result is compared to the reference experimental curve of $\eta_p^{ref}\left(t,T\right)$ for $T_i = 465$°C, 530°C or 600°C and at the different times of the experimental measurements $t^{(j)}$ using a cost function $\mathcal{F}$:

$$\mathcal{F} = \sum_{i,j} \left(\eta_p^{ref}\left(t^{(j)}, T_i\right) - \eta_p\left(t^{(j)}, T_i\right)\right)^2 \tag{13}$$

- a variation is introduced on the values of P

The iterative process is stopped as the cost function reaches a minimum.
As a preliminary to the identification process, a quantitative sensitivity analysis has been performed on the parameters of the model. It is presented in Appendix D. It consists in testing different sets of parameter $P = \{a_1, a_2, \tau, n\}$ and in quantifying the effects of their variations on the computed porosity content. This sensitivity analysis shows that any of these parameters have a significant influence which validates the relevance of the proposed form of $G\left(t,T\right)$. It also enables to determine a reference set of parameters. This iterative process was started from this reference set.
The identified parameters are presented in Table 1. The quality of this identification was then validated by comparing the computed kinetics of porosity formation at $T = 500$°C to the experimental one through a Euler scheme. Furthermore, a Monte-Carlo method was used on a large amount of elements to verify that similar porosity content were obtained. All the computed curves of $\eta_p\left(t,T\right)$ can be compared to the experimental ones on Fig. 9. Some caution should be taken with temperatures exceeding 600°C as oxidation starts to occur, which alters the internal structure of the yarn, and is not considered by the model.

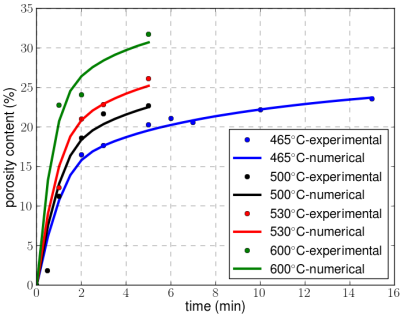

Figure 9: Comparison of the experimental / numerical evolution of the porosity content over time of η_p^* for different temperatures of exposure

3.2.4. Probability law: adapted form

Modelling both thermal transfers and mechanical fields under a mechanical load involves dealing with non-linearities originating from the gradients of properties according to temperature and constituent. To this respect, for a good trade-off between accuracy of the porosity kinetics description and efficiency of the numerical analyses, Δt should lie within a range from 10s to 60s. Let the relative error RE of a function f to a reference value f^{ref} be defined as:

$$RE\left(f\right) = \left| \frac{f - f^{ref}}{f^{ref}} \right| \times 100 \tag{14}$$

Computing $RE\left(\int_0^t \eta_p\left(t,T\right) dt\right)$ for different values of Δt, and taking the reference solution as that obtained with $\Delta t = 10^{-3}$s, it is shown that the error becomes significant for time increments larger than 1s, as seen from Fig. 10a.

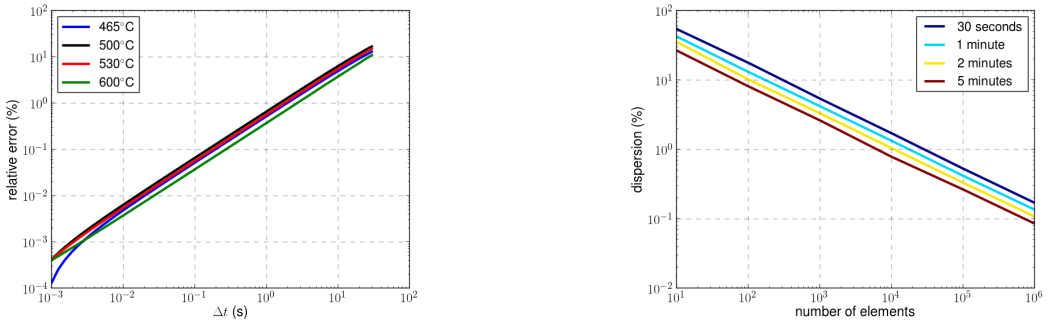

(a) (b)

Figure 10: Theoretical error and deviation of the porosity nucleation law. (a) Evolution of the relative error of $\int_0^t \eta_p\left(t,T\right) dt$ according to Δt for different temperatures of exposure. The reference solution is the one obtained with $\Delta t = 10^{-3}$s. (b) Evolution of the deviation of the porosity content from to the theoretical asymptotic value according to the number of initial matrix elements N_m^0 for different exposure times at 530°C

This error originates from the inherent error introduced by the Euler scheme as the small Δt criterion is no longer met. In order to enable the use of $\Delta t \geq 10$s, the definition of $p\left(t,T,\Delta t\right) = G\left(t,T\right)\Delta t$ must then be corrected with an adaptation function $f_a\left(\Delta t\right)$. The expression of $f_a\left(\Delta t\right)$ and the explanations on its definition are provided in Appendix C. This Appendix also presents an analysis on the robustness of the adapted form, showing that results do not depend on Δt, provided it be lower than 60s.
Given the high time-rate of evolution of the porosity content as obtained experimentally, even for the lowest temperature causing the polymer matrix decomposition, Δt larger than 60s would lead to a lack of accuracy. Therefore this upper bound of Δt is not the source of any reduction in the efficiency of the thermomechanical computations.

3.2.5. Sensitivity to mesh size

As the probabilistic approach consists of a series of random draws, a bias might be introduced if the amount of elements is not large enough as it would not result in representative values of the asymptotic behavior. Eq. 9 was used to assess the convergence of the probability-based $\eta_p\left(t,T\right)$ according to the number of elements N_m^0 used. An arbitrary setting of $T = 530$°C and $\Delta t = 30$s was chosen. Let the deviation from the theoretical value $\eta_p^\infty\left(t,T\right)$ be defined as $d\left(N_m^0,t,T\right) = RE\left(\eta_p\left(t,T\right)\right)$. As explained in Appendix E, $d\left(N_m^0,t,T\right)$ at a given temperature T and a given time t can be expressed according to Eq. 15, where p is the probability of nucleation at the considered time and temperature.

$$d\left(N_m^0\right) = \left(\frac{100}{\pi}.\frac{1-p}{pN_m^0}\right)^{\frac{1}{2}} \tag{15}$$

Fig 10b shows the variation of d according to N_m^0 for four exposure times at 530°C. Results show that the porosity content is only lightly affected by the number of elements. It appears that for a model with 10^6 elements, the dispersion is lower than 0.1%. As a realistic amount of matrix elements would be of this

magnitude, it can be assumed that the randomness is limited to the location of porosity nucleation and does not reflect at the macroscopic scale.
A view on the decomposed subdomain is shown on Fig. 11 for two different refinements. The coarsest mesh corresponds to the one used in [21] for the determination of the laminates axial stiffness evolution in the temperature range from the ambient to the onset of decomposition T_d. Whereas this mesh was fine enough to predict thermoelastic properties of the laminates up to T_d, this qualitative comparison tends to show that the analyses for $T \geq T_d$ are more demanding in terms of mesh size refinement. Further analyses on mesh size effect, from the quantitative point of view, are presented in section 3.3.

3.3. Porosity-induced swelling

In order to reproduce the observed macroscopic swelling-induced expansion of the laminates, the simulation of porosity formation has to be completed by a mechanical simulation to include the mechanism of swelling at the scale of porosities. As to mimick a gas, a void is treated as a solid isotropic elastic material with a Young Modulus of 10^{-3}MPa. The fiber bundles and the matrix are assigned the same mechanical properties as those used in the previous work [21]:

- temperature-independent isotropic transverse elasticity for the fiber bundles; it is assumed that oxidation of the fibers does not occur;
- temperature-dependent isotropic elasticity for the matrix; in the molten state, its Young Modulus is set at 1MPa; it corresponds to the upper bound below which the set value does not impact the mechanical properties of the laminates, as explained in [21].

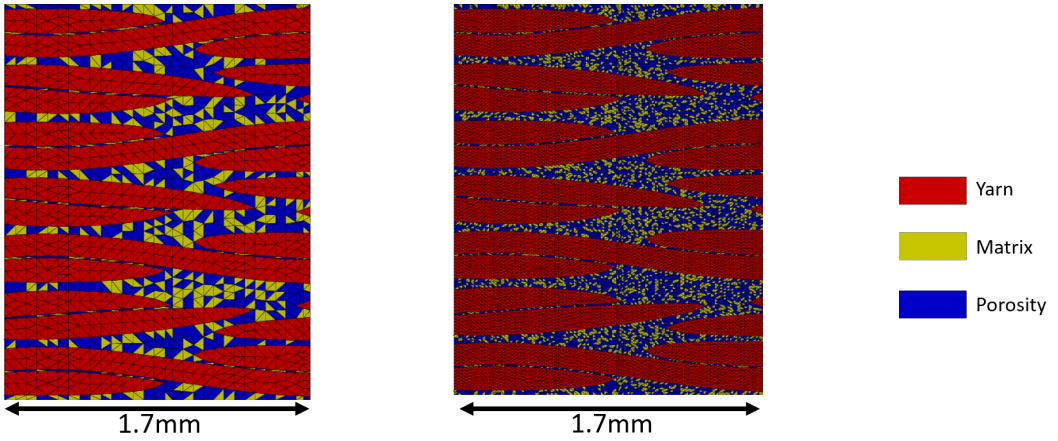

(a) (b)

Figure 11: Simulation of the thermally induced porosity formation in the laminates at 530°C for 5 minutes with explicit porosity distribution. (a) coarse mesh (b) refined mesh

In this configuration, the value of the imposed internal pressure becomes the only input governing the extent of the macroscopic swelling-induced expansion. Before addressing the question on how the value of the internal pressure was adjusted, a preliminary attention needs to be paid to the effect of mesh refinement. Fig. 12 shows the geometry of the subdomain in its swollen state after a 5 minute exposure at 530°C for two mesh refinements. With the coarse mesh (corresponding to that in [21]), the large size of the voids is at the origin of significant irregularities in the geometrical representation of the fiber bundles. A fine enough mesh, e.g. such as the one in Fig. 12(b), should thus be used in order to minimize the sources of artifacts in the thermomechanical modelling during the matrix decomposition.
Having defined the mesh refinement, further analyses were conducted on the qualitative effect of the imposed pressure on the thickness expansion. As a consequence of the rapide decrease of the matrix rigidity upon temperature increase, it was observed that the imposed internal pressure should be defined as a function decreasing through time at rates depending on the temperature of exposure. This function further needs to converge to a saturated value, such as to reproduce the stabilization of the thickness expansion to a constant value.

Let us note P_{int} this imposed internal pressure. The form of P_{int} given in Eq. 16 enables to describe these trends:

$$P_{\text{int}}(t) = D_1 exp\left(-D_2 (t-1)^{D_3}\right) + D_4 \tag{16}$$

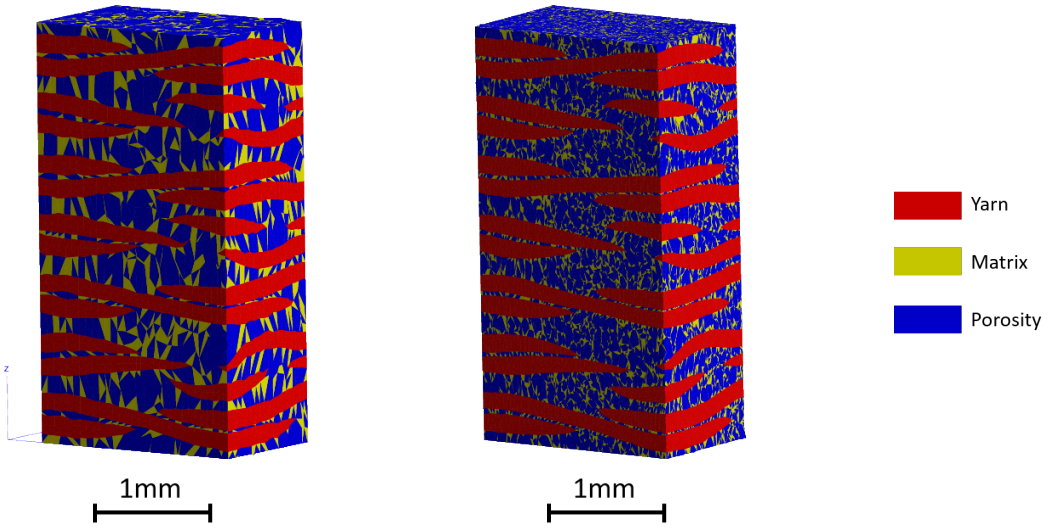

Figure 12: Simulation of the porosity induced swelling on the laminates thermally decomposed for 5 minutes at 530°C. (a) coarse mesh (b) fine mesh

$(D_i)_{i=1,\ldots,4}$ are constant parameters which enable to introduce the dependencies to the temperature of exposure. Table 2 defines their respective roles and provide the values which were identified. Fig. 13 presents the simulated evolution of thickness expansion over time for three temperatures of exposure, to be compared with the experimental measurements.
The form which has been set for $P_{\text{int}}(t)$ is certainly arbitrary, but it produces a phenomenology which is consistent with physics. And Fig. 13 shows that the modelling thereby constructed is capable of correctly representing thickness expansion evolutions for different temperatures of exposure.

Parameter	Unit	Temperatures			Main role
		465°C	530°C	600°C	
D_1	Pressure (MPa)	0.836	0.590	1.82	Value of P_{int} at the initial time
D_2	Rate (s^{-1})	0.289	3.38	1.23	Dependence of P_{int} to t at the initial time
D_3	No unit	2.05	1.66	1.66	Dependence of P_{int} to t at the intermediate times
D_4	Pressure (MPa)	1.31	1.34	0.320	Asymptotic value of P_{int}

Table 2: Parameters used to define $P_{\text{int}}(t)$ as given by Eq. 16

4. Discussion

4.1. Case of a homogeneous temperature

First, it should be recalled that the present modelling is aimed at describing how through thickness thermal transfers and polymer matrix decomposition evolve concurrently during one-sided thermal irradiation of the laminates. This description is a prerequisite for any representation of the load transfers and their consequences on the degradation of the mechanical properties of the laminates over time. It requires an accurate spatio-temporal representation of the porosity formation process. Its motivation is not so much to account for thermodynamics based mechanisms of solid-state transformations, but to reproduce the phenomenology of porosity formation kinetics at the mesoscale of the laminates. This is the reason why thermal decomposition mechanims, as enclosed in the modelling, are not fully representative of the involved physico-chemistry. Instead, they are locally incorporated in the numerical modelling according to a phenomenological time and

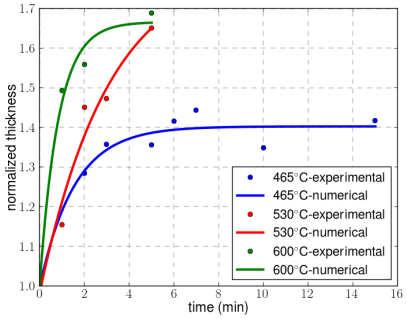

Figure 13: Comparison experimental / numerical of the thickness expansion evolution over time for the different temperatures of exposure

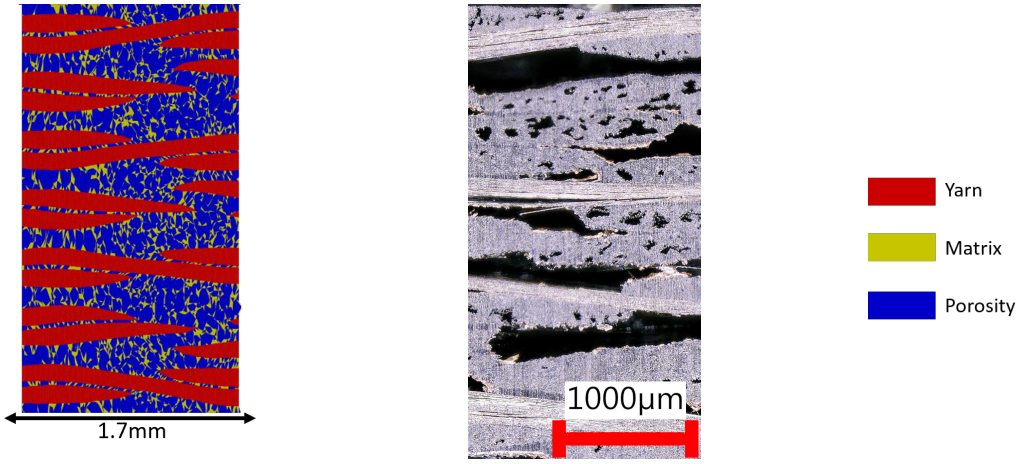

(a) (b)

Figure 14: Observation of the porosity distribution on the contour of the laminates exposed to 530°C during 5 min: (a) as simulated, (b) as observed from SEM

temperature dependent probabilistic law.
Such an approach have shown its ability and robustness to reproduce both the evolution of the porosity content at different temperatures and the swelling induced expansion. Limitations were found for high temperatures (around 530°C) and times (over 5 minutes), when the laminates collapses. This phenomenon is due to internal structural effects associated with the decomposition of fiber bundles. Neither this intra-bundle decomposition mechanism nor its consequences are included in the numerical model. Such improvements will be the subject of future modelling developments.
From a qualitative point of view, the porosities were found to be homogeneously distributed within the laminates after swelling. This can be compared to micrographs of the laminates decomposed with same temperature (530°C) and time of exposure (5 min), as provided in Fig. 14a and 14b. Two kinds of porosities are observed experimentally: small ones, heterogeneously distributed, as in the simulation, and large ones. In order to obtain these from numerical modelling, it is necessary to introduce two additional mechanisms of porosity formation: growth and coalescence. This corresponds to the next step of modelling development. The tendency for porosities to nucleate at the matrix/fiber bundle interface was also noted. However, as the current approach results in an accurate porosity content and swelling induced expansion, it fulfils the two main requirements for a correct prediction of the thermal properties evolution of the laminates under thermal irradiation.

4.2. Case of a thermal gradient

For a homogeneous distribution of temperature within the laminates, porosities appear and develop in different forms and according to different processes: voids of various sizes formed from nucleation, growth

and coalescence, and matrix-fiber bundle decohesion due to the contrast in thermal expansion properties. Whatever their nature, their spatial distributions are homogeneous within the laminates as can be observed on Fig. 3. It would thus be possible to include their effect on the thermomechanical properties by means of a state variable in the constitutive laws, such as *e.g.* in the GTN model. But in the circumstances of a thermal gradient, considering the high contrast in thermal properties between the three constituents (matrix, fibers and porosities) combined to the highly heterogeneous spatial arrangement of fiber bundles and matrix, an explicit account of porosities locations must be made. This justifies the meso-structure based approach with an explicit representation of porosities within the laminates and this corresponds to the final case of study hereafter.

The case of a 115kW/m^2 heat flux imposed on the top surface during 90s has been considered. Radiation and convection heat transfers were set on the bottom surface. Sides were considered adiabatic to simulate the case of a small domain embedded into a larger one. The boundary conditions as well as the thermal properties of the components are detailed in Carpier et al. [21].

Fig. 15 presents the distribution of porosities on the contour of the mesh with or without accounting for the porosity swelling. Both gradients of decomposition and swelling correctly compare with those observed experimentally in the same conditions of irradiation (see Fig 1).

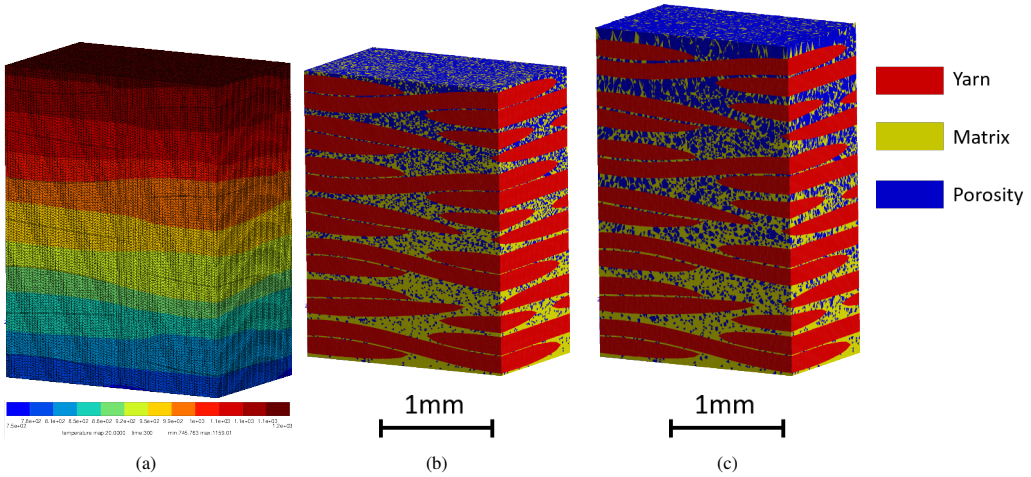

Figure 15: Example of a heterogeneous temperature decomposition simulation after exposure to a 115kw/m^2 heat flux for 90s (a) temperature field (°C) ,(b) before swelling ,(c) after swelling

From this full-field representation of thermal transfers and porosities it is possible to extract characteritic measurements of the state of the laminates; firstly from ply to ply in Fig. 16a, which depicts the mean temperature and induced swelling per ply, highlighting the decomposition state reached in the different plies of the laminates.

Out-of-plane displacement and porosity content show an overall tendency to increase from one ply to the other the higher the temperature becomes, see Fig. **??**. However it is drastically inhomogeneous within each ply. This heterogeneity originates from the mesostructure of the plies, as the matrix is in majority located on the lower and upper parts of each pristine ply. As a result, the porosity content as well as the out-of-plane displacement are much higher at the ply borders.

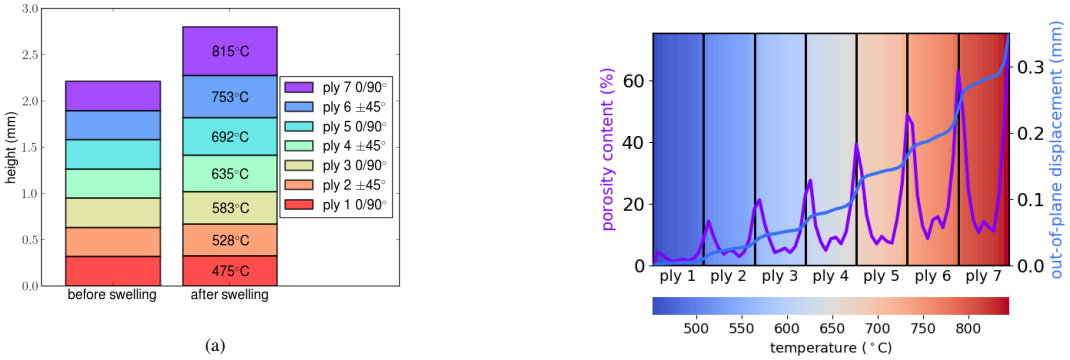

(a)

Figure 16: Simulation of the exposure to a 115kw/m^2 heat flux for 90s: (a) schematics of the out-of-plane swelling and average temperature, (b) evolution of the out-of-plane displacement and porosity content in each plies

5. Conclusions

Under the conditions of a one-sided exposure to a high thermal energy source such as a flame, the tensile strength of a polymer matrix composite laminates is considerably reduced, but it can remain significant for a period of time long enough to avoid a catastrophic outcome. One of the major degradations in thermomechanical properties occurs during the pyrolysis of the matrix. This article is aimed at presenting an original modelling of this progressive thermal decomposition of the polymer matrix within a composite laminate, following different stages:

- Accurately describe the thermal gradients
- Reproduce the kinetics of porosity formation during the thermal decomposition of the matrix to account for the rapid and dramatic evolution of the polymer state
- Explicitly represent the presence of voids acting as thermal insulators
- Create a model compatible with further coupled thermomechanical considerations

Thus, a comprehensive set of experimental analyses has been performed in the regime of polymer matrix decomposition (homogeneous temperature above that of polymer decomposition) for C/PPS laminates. These analyses highlighted the rapidity of the porosity formation process and its strong dependence on exposure temperature. For the targeted case of strong thermal gradients, this first implies having a reliable kinetics law of porosity formation over the entire temperature range involved. Secondly, a representation of void formation at the local scale of the laminate must be possible. A meso-scale FE model where fiber bundles and matrix are explicitly represented has thus been adopted; a kinetics law has been developed and identified from the experimental analyses; each finite element of the matrix phase were attributed temperature dependent thermal properties and a probability of nucleation determined from the kinetics law; the process of thermally driven transformation of a matrix element from solid to glassy, liquid and gas were further completed by the application of an internal pressure to reproduce the mechanism of blunting due to pyrolysis gases.
The model replicates correctly the porosity content within the laminates as a function of time and temperature as well as the thickness expansion. It has demonstrated its ability to reproduce a gradient of polymer decomposition through the thickness of the laminates and the corresponding gradient of the swelling from one ply to another. The precision of the meso-scale approach highlights intra-ply inhomogeneity.
It ultimately provides the necessary inputs to tackle the strongly coupled thermomechanical problem of stress redistribution within a single-sided thermally irradiated laminates.
This problem is particularly relevant in the case of a flame exposure, where, as the literature shows, the thermomechanical states evolve very rapidly and involve the coexistence of dramatically decomposed plies close to the flame and slightly degraded ones on the opposite side. It is expected that these differences in the thermal decomposition of the plies result in significant changes in terms of load bearing capabilities.

Appendix A. Measurement methods

Experimental protocols were considered to understand the kinetics associated with the porosity formation, both at qualitative and quantitative levels:

- Qualitative analyses: Optical microscopy, X-Ray tomography
- Quantitative analyses: Geometrical measurements, mass measurements, densitometry

The qualitative study focuses on the spatial distribution, shape and dimensions of porosities according to time of aggression while the quantitative one aims at measuring the amount of porosities within the laminates.The perfect analysis would result in a further understanding of both the explicit spatial distribution of the porosities and the amount of porosities in the laminates, which is the case of X-Ray tomography. However it was restrained to qualitative considerations. Indeed, the cost of analysis is not compatible with the current objectives of a modelling development: it requires a large amount of samples to cover the representative time and temperature ranges involved in the decomposition of the laminates. Therefore, in order to constitute the reference set of experimental measurements necessary for a comprehensive identification, a more simple and efficient experimental protocol was applied to determine experimentally the porosity content (a volume fraction), noted $\eta_p\left(t,T\right)$.
As the composite material is subjected to thermal decomposition, the nucleated porosities induce the presence of high-pressure gas pockets which, as they expand, introduce an increase of the volume of the macrostructure through the peeling of laminates plies. The volume increase (quantitative) and cavity distribution (qualitative) were studied by the experimental means described thereafter. Stationary and isothermal conditions were considered: samples are deposited in a muffle furnace (Nabertherm, inside volume inertia of $29 \times 30 \times 18\text{cm}^3$) at a stabilized temperature T; given the thermal inertia of the furnace (temperature back to the setpoint in less than 10 seconds) and the small dimensions of the samples, the time of heating of the sample is considered negligible compared to the characteristic times of the decomposition analyses ($\sim$ 1min) and the sample can reasonably be assumed to reach the target temperature instantaneously and uniformally. Each measurement was repeated three times on three different samples giving a reference value of the porosity content at time t and temperature T, noted $\eta_p^{ref}\left(t,T\right)$, as well as its variance.
Five different experimental techniques were employed: (i) mass loss (ii) densitometry (iii) geometry (iv) optical microscopy observation (v) X-Ray tomography. They can be divided into two categories: on the one hand (i), (ii) and (ii) rely on measurements of samples before and after they were subjected to thermal aggression. This allows the porosity content to be calculated as the ratio of porosity volume over the final volume after swelling. On the other hand, (iv) and (v) rely on post-mortem observations in which the porosities are directly detected by visual means. All five experimental methods are detailed below.

Appendix A.1. Mass loss

This technique is solely based on mass measurements. The mass of the sample is measured before and after thermal exposure. Let us note (i) $m_{\#}^{\star}$ the mass of the considered material $\#$ (either fiber, matrix or composite laminates) at the state defined by $\star$ (either initial or decomposed), (ii) η_m^{ini} and η_f^{ini} the volume fractions of matrix and fibers within the laminates at the initial state, and (iii) ρ_m and ρ_f the densities of the matrix and the fibers. The porosity content can be expressed as:

$$\eta_p = \left(1 - \frac{m_{cl}^d}{m_{cl}^{ini}}\right)\left(\frac{m_m^{ini} - m_m^d}{\rho_m} + \frac{m_f^{ini} - m_f^d}{\rho_f}\right)\frac{\eta_m\rho_m + \eta_f\rho_f}{m_{cl}^{ini} - m_{cl}^d} \tag{A.1}$$

In the present case, since $\eta_m = \eta_f = 0.5$, and by considering that the mass loss only comes from the matrix, Eq.A.1 can be simplified into:

$$\eta_p = \frac{\left(1 - \frac{m_{cl}^d}{m_{cl}^{ini}}\right)\left(\rho_m + \rho_f\right)}{2\rho_m} \tag{A.2}$$

Its main drawback is that it does not provide any information on the swelling of the laminates.

Appendix A.2. Densitometry

This technique uses a densitometric scale. It consists in measuring the weight of a sample in the air then in water and then in applying Archimedes formulas in order to determine the density. With m_{cl}^a the mass of the composite laminates in the air, m_{cl}^w the mass in water and ρ_a, ρ_w the density of respectively air and water, the density of the sample is

$$\rho_{cl}^d = \frac{m_{cl}^a}{m_{cl}^a - m_{cl}^w} (\rho_w - \rho_a) + \rho_a \tag{A.3}$$

The density of the sample is calculated before and after thermal exposure. Knowing both its density and its mass, its volume can be determined and the volume difference originates from the porosity formation. The results are however strongly influenced by edge effects as the edges become thicker than the center. Indeed, after a 5 minute exposure at 530°C, the thickness increase is mainly located within five millimetres from the edges and up to 30% higher. The density is therefore lower on these parts of the sample and it can reduce the laminates density down to a value lower than 1. In this case, the density formula from Eq. A.3 is then altered and given by A.4.

$$\rho_{cl}^d = \frac{m_{cl}^a \rho_w}{m_{cl}^a - m_{cl}^w} \tag{A.4}$$

Noting ρ_{cl}^{ini} and ρ_{cl}^d the initial and final densities of the sample, the porosity content finally reads:

$$\eta_p = \frac{m_{cl}^d/\rho_{cl}^d - m_{cl}^{ini}/\rho_{cl}^{ini}}{m_f^{ini}/\rho_f} \tag{A.5}$$

Appendix A.3. Geometry

This technique is based on the measurement of the initial (V_{cl}^{ini}) and final volumes (V_{cl}^d) of the samples. The porosity volume is finally obtained by adding the contributions of both the closed and open porosities (see subsection 2.2 for the open/closed distinction). The contribution of the former is the volume difference between the onset and after exposure. This accounts for the swelling of the material. The contribution of the latter is the mass lost during the process as the pyrolysis gas escape. Ultimately, the porosity content reads

$$\eta_p = \frac{V_{cl}^d - V_{cl}^{ini}}{V_{cl}^d} + \frac{m_{cl}^{ini} - m_{cl}^d}{\rho_m V_{cl}^d} \tag{A.6}$$

Edges effects (increase in thickness on the borders) may affect the measurements, similarly to densitometry. However they were avoided by measuring the dimensions at the center of the sample.

Appendix A.4. Optical microscopy

This technique relies on destructive observations. Once the sample has been thermally decomposed, it is cut into 3mm-height slices. These profiles are then observed and captured using a 3D numerical microscope (KEYENCE VHX-500). Images are finally numerically treated in order to compute the porosity surface fraction. This method highly depends on both the localisation of the cut and the segmentation threshold chosen by the user. Furthermore, the black/white threshold presents some subjectivity as it is set by the user to detect the porosities where they are likely to appear. It is also expected that the cutting process reduces the porosity area, hence decreasing the porosity content.

Appendix A.5. X-Ray tomography

This last technique uses 3D reconstruction (software 3D slicer) of tomography slices (EasyTom 150, $9.5\mu m$, 150kV) to isolate and dissociate the porosities within the material. As for the optical microscopy method, a segmentation threshold is used, with the same drawback. But since the whole volume is considered, the disparity between measurements is reduced.

After comparison of these techniques, it was chosen to quantify $\eta_p\,(t, T)$ using the geometry based method for the case of homogeneous thermal exposure. The porosity contents obtained with the first four methods for the samples of Fig. 3 are presented on Table A.3. It highlights the clear underestimation of the mass

loss and optical microscopy methods, and the unreliability of the densitometry method (at 530°C) due to the possible edge effects.

	Geometry	Mass loss	Densitometry	Optical microscopy
465°C-7min	28.6%	2.2%	29.9%	9.4%
530°C-7min	43.2%	8.9%	66.2%	25.9%
600°C-5min	54.8%	24.2%	51.3%	47.9%

Table A.3: Porosity contents of the samples of Fig. 3 as obtained by geometry, mass loss, densitometry and optical microscopy methods

X-Ray tomography and optical microscopy were however used to analyse the porosity formation process from a qualitative standpoint. It is to be noted that the technique based on geometrical measurements is relevant only for scenarii of homogeneous temperature. In the case of decomposition gradients, tomography and microscopy have to be used in a quantitative way, with a special attention to the representativity of the results in terms of edge effects as well as 2D projection in the microscopy method.

Appendix B. Experimental analysis protocol

Throughout the experimental analyses, the following protocol was applied:

- Preparation of $25 \times 25 \times 2.2\text{mm}^3$ samples (water cutting, cleaning, drying)
- Initial measurements (geometry, mass measured three times and averaged)
- Exposure in the muffle furnace at the setpoint temperature
- Removal of the sample after a given exposure time
- Post-mortem measurements at the center of the samples to prevent edge effect influence
- Use of three samples for each (time,temperature) set

Temperatures and times of exposure were carefully chosen to provide the wider possible range of results. Thermal decomposition tests were carried out for the following constant temperatures:

- 465°C: slightly above the onset of the thermal decomposition [1]
- 500°C and 530°C: intermediate temperatures which represent intermediate trends in terms of porosity content
- 600°C: temperature limit for post-mortem observations

Exposure times were set at various times highlighting the primary kinetics changes up to 15 minutes (FAA standards resistance time [32]).

Appendix C. Detailed time increment adaptation function

The corrected nucleation probabilistic law reads:

$$p\left(t,T\right) = G\left(t,T\right)\Delta t \times f_a\left(\Delta t\right) \tag{C.1}$$

The time increment correctional factor $f_a\left(\Delta t\right)$ is expressed as:

$$f_a\left(\Delta t\right) = \frac{1}{\left(0.833 + \left(0.00458 - 0.00167\left(\frac{T - T^{ref}}{T^{ref} - T_d}\right)\right)\left(\Delta t^{ref} - \Delta t\right)\right)} \tag{C.2}$$

The reference Δt^{ref} was set at 30s as to conveniently fit the experimental data while not being too large to capture progressive mesostructural changes. Fig. C.17 shows the good agreements for various time increment values up to 60s.

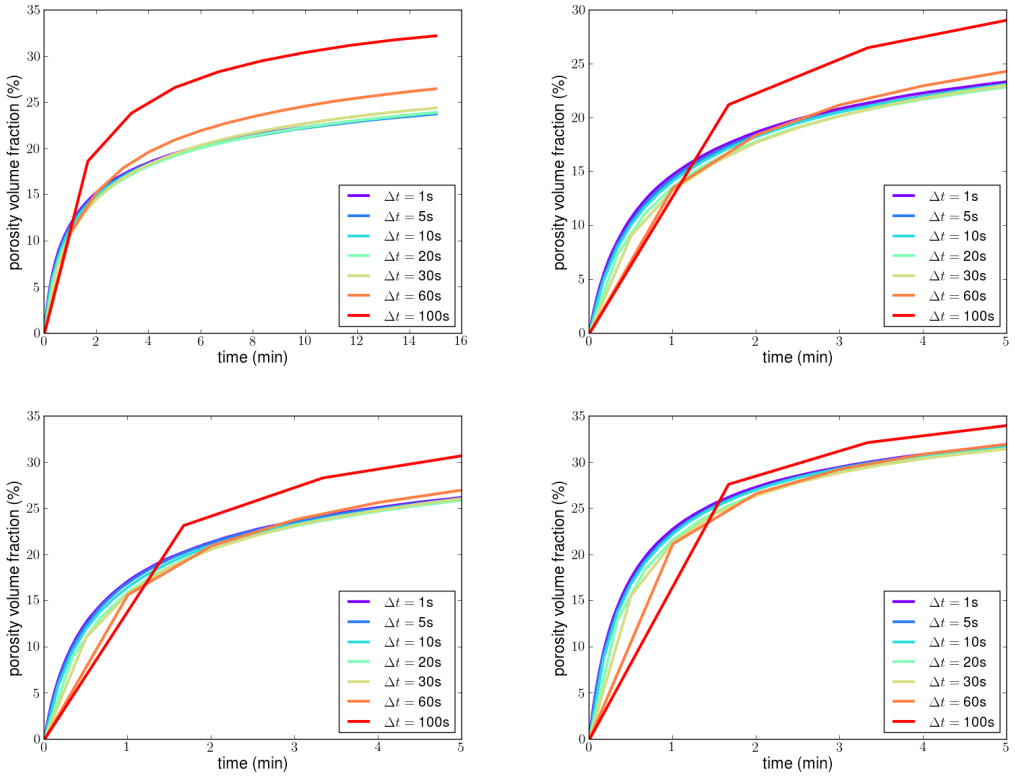

Figure C.17: Influence of the dt value on $\eta_p\left(t,T\right)$ at 465°C, 500°C, 530°C and 600°C

Appendix D. Sensitivity analysis on the nucleation probabilistic law parameters

Let P be the set of parameters with $P_{i,0} \in \{a_1, a_2, \tau, n\}$. It was chosen to investigate the influence of the factors on the resulting porosity content by considering an arbitrary variation interval for each parameter so that $P_i \in [\frac{1}{2}P_{i,0}, 2P_{i,0}]$ introducing parameter factors $F_i \in [0.5, 2]$. The porosity content therefore depends on F_i, T and t and can be noted $\eta_p^i\left(t,T\right)$. Two approaches were considered, having either the temperature or the time set and the other varying to investigate the influence of the parameters on each:

- $\eta_p^i\left(T,t\right)$ was calculated according to time or temperature for various parameter factors . The dispersion $d^i\left(t,T\right)$ around the reference probability law $\eta_p^{i,0}\left(T,t\right)$ was defined as $d^i\left(t,T\right) = RE\left(\eta_p^i\left(t,T\right)\right)$. The amount of parameter factors was limited to two for curve readability, chosen as the boundaries 0.5 and 2.

- For a complete overview of the parameter factors, the $\eta_p^i\left(T,t\right)$ were integrated over time (at fixed temperature) or over temperature (at fixed time) such as $S^i\left(F_i,T\right) = \int_0^{t_{final}} \eta_p^i\left(T,t\right)dt$ and $S^i\left(F_i,t\right) = \int_0^{t_{final}} \eta_p^i\left(T,t\right)dT$. The dispersion around the reference integral value $S^{i,0}\left(F_i,t\right)$ according to the chosen parameter factor $D^i\left(F_i,t,T\right)$ was defined as $D^i\left(F_i,T\right) = RE\left(S^i\left(F_i,T\right)\right)$ and $D^i\left(F_i,t\right) = RE\left(S^i\left(F_i,t\right)\right)$.

Specific cases representative of the general tendencies are presented with set temperature of 600°C and times of 50s, 100s and 300s.
Fig. D.18 to D.25 quantify the impact of said parameters according to time and temperature. Results highlight the major dependence in either time or temperature for each parameter, justifying the need for a precise estimate.

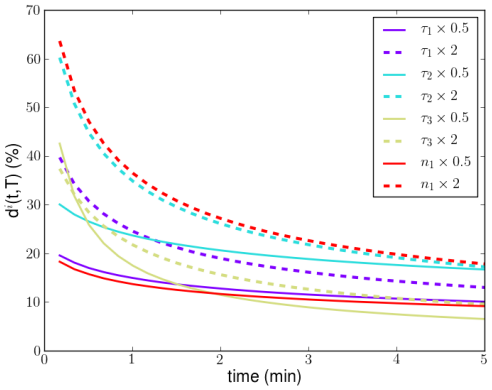

Figure D.18: Influence of parameter values on $d^i\ (t, T)$ according to time at 600°C

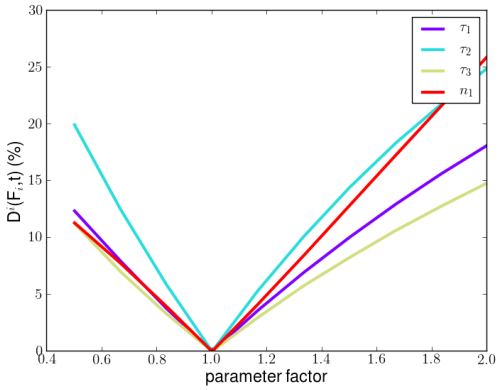

Figure D.19: Influence of parameter values on $D^i\ (F_i, t)$ according to time at 600°C

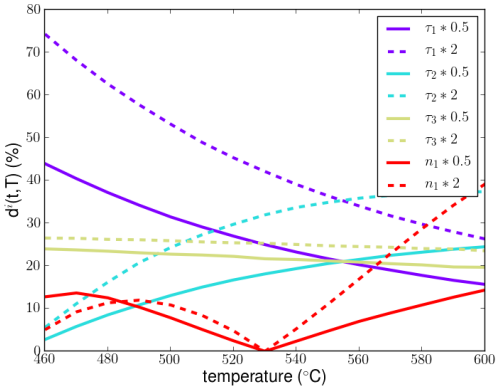

Figure D.20: Influence of parameter values on $d^i\ (t, T)$ according to temperature after 50s

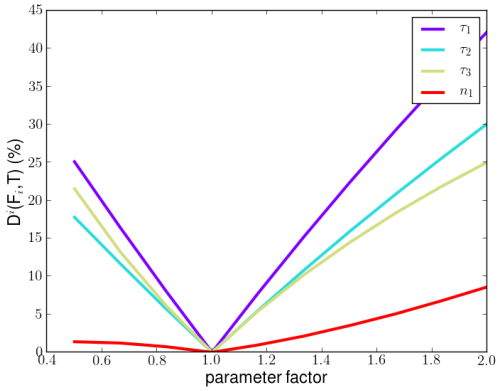

Figure D.21: Influence of parameter values on $D^i\ (F_i, T)$ according to temperature after 50s

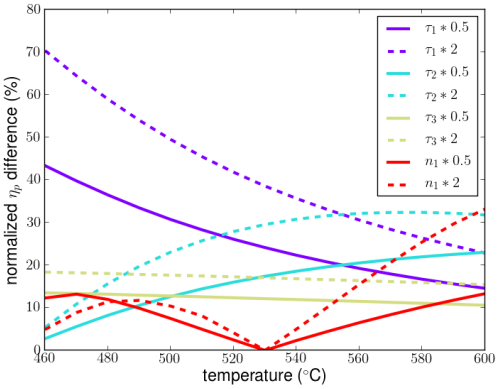

Figure D.22: Influence of parameter values on $d^i\ (t, T)$ according to temperature after 100s

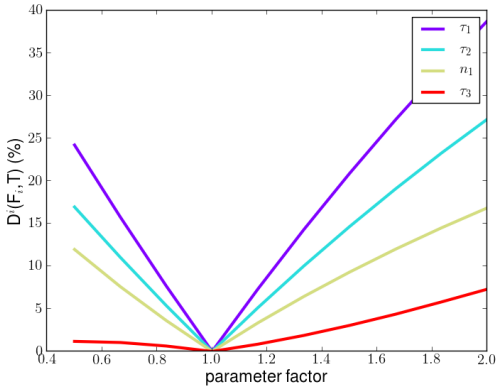

Figure D.23: Influence of parameter values on $D^i\ (F_i, T)$ according to temperature after 100s

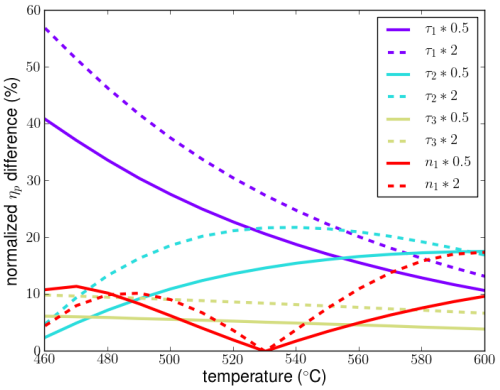

Figure D.24: Influence of parameter values on $d^i\ (t, T)$ according to temperature after 300s

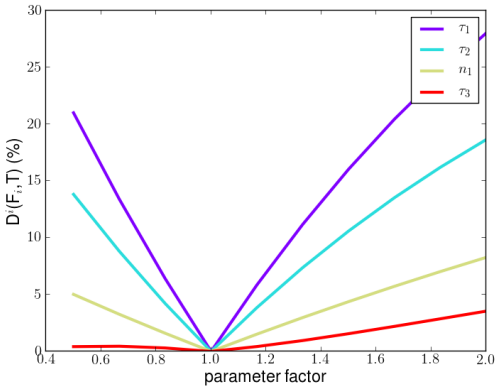

Figure D.25: Influence of parameter values on $D^i\ (F_i, T)$ according to temperature after 300s

Appendix E. Identification of the linear parameters of the dispersion / number of elements relation

As each matrix element undergoes a Bernoulli trial at each time step with a probability $p(t,T)$ to turn into a porosity, the porosity content follows a step-by-step binomial random variable $B(n,p)$. Let X_n be the amount of successes out of n possibilities so that the probability of achieving it reads

$$P(X_n = k) = \binom{n}{k} p^k (1-p)^{n-k} \tag{E.1}$$

Let the mean relative deviation $D_n(p)$ be defined as

$$D_n(p) = \mathbb{E}\left(\frac{|X_n - \mathbb{E}(X_n)|}{\mathbb{E}(X_n)}\right) \times 100 \tag{E.2}$$

As for a binomial distribution $B(n,p)\ \mathbb{E}(X_n) = np$, De Moivre showed in 1730 that $D_n(p)$ can be expressed as

$$\begin{aligned} D_n(p) &= 2n\binom{[np]}{n-1} p^{[np]+1} (1-p)^{n-[np]} \times \frac{100}{np} \\ &= \frac{2n\,(n-1)!}{[np][np]!\ (n-np-1)!} p^{[np]+1} (1-p)^{n-[np]} \times \frac{100}{np} \end{aligned} \tag{E.3}$$

As n tends toward high values, Stirling's formula stipulates that $n!$ can be approximated as

$$log(n!) \approx n\,log(n) - n + \frac{1}{2} log(2\pi n)$$

. After application of Stirling's formula and developments, Eq. E.3 becomes

$$log(D_n(p)) = -\frac{1}{2} log(n) + \frac{1}{2} log\left(200\frac{1-p}{2\pi p}\right) \tag{E.4}$$

For a calculation at 30s, numerical application renders the line equation $log(D_n(p)) = -\frac{1}{2} log(n) + 2.11$ which corresponds to what is observed on Fig. 10b. It is to be noted that for n values lower than a 100, slight differences appear between the numerical and theoretical values as Stirling formula's assumption of a large N is no longer met.

References

[1] C.-C. M. Ma, H.-C. Hsia, W.-L. Liu, J.-T. Hu, Studies on thermogravimetric properties of polyphenylene sulfide and polyetherether ketone resins and composites, Journal of Thermoplastic Composite Materials 1 (1) (1988) 39–49. arXiv:https://doi.org/10.1177/089270578800100104, doi:10.1177/089270578800100104.

[2] Y. Carpier, B. Vieille, A. Coppalle, F. Barbe, Study of thermomechanical coupling in carbon fibers woven-ply reinforced thermoplastic laminates: Tensile behavior under radiant heat flux, Polymer Composites 41 (9) (2020) 3552–3563. arXiv:https://onlinelibrary.wiley.com/doi/pdf/10.1002/pc.25641, doi:https://doi.org/10.1002/pc.25641.

[3] Y. Carpier, A. Alia, B. Vieille, F. Barbe, Experiments based analysis of thermal decomposition kinetics model. case of carbon fibers polyphenylene sulfide composites, Polymer Degradation and Stability 186 (2021) 109525. doi:https://doi.org/10.1016/j.polymdegradstab.2021.109525.

[4] P. Zuo, A. Tcharkhtchi, M. Shirinbayan, J. Fitoussi, F. Bakir, Overall investigation of poly (phenylene sulfide) from synthesis and process to applications—a review, Macromolecular Materials and Engineering 304 (5) (2019) 1800686. arXiv:https://onlinelibrary.wiley.com/doi/pdf/10.1002/mame.201800686, doi:https://doi.org/10.1002/mame.201800686.

[5] L. C. Lopez, G. L. Wilkes, Poly(p-phenylene sulfide)—an overview of an important engineering thermoplastic, Journal of Macromolecular Science, Part C 29 (1) (1989) 83–151. arXiv:https://doi.org/10.1080/07366578908055165, doi:10.1080/07366578908055165.

[6] G. Chen, A. K. Mohanty, M. Misra, Progress in research and applications of polyphenylene sulfide blends and composites with carbons, Composites Part B: Engineering 209 (2021) 108553. doi:https://doi.org/10.1016/j.compositesb.2020.108553.

[7] J. Aucher, Etude comparative du comportement composites à matrice thermoplastique ou thermodurcissable, Ph.D. thesis, INSA de Rouen (2011).

[8] S. Feih, A. Mouritz, Tensile properties of carbon fibres and carbon fibre–polymer composites in fire, Composites Part A: Applied Science and Manufacturing 43 (5) (2012) 765–772, office of Naval Research (ONR): Composites in Fire. doi:https://doi.org/10.1016/j.compositesa.2011.06.016.

[9] J. Bibinger, S. Eibl, H.-J. Gudladt, Influence of low and extreme heat fluxes on thermal degradation of carbon fibre-reinforced polymers, Applied Composite Materials 29 (5) (2022) 1817–1840.

[10] T. M. Vetter, S. Eibl, H.-J. Gudladt, Predicting delaminations and residual strength of carbon fibre reinforced polymers (cfrp) after one-sided thermal loading by means of infrared spectroscopy, Applied Composite Materials 28 (2) (2021) 427–446.

[11] S. Duquesne, S. Bourbigot, Char Formation and Characterization, 2009, pp. 239–259. doi:10.1201/9781420084009-c10.

[12] S. C. Moldoveanu, Chapter 2 thermal decomposition of polymers, in: Analytical Pyrolysis of Synthetic Organic Polymers, Vol. 25 of Techniques and Instrumentation in Analytical Chemistry, Elsevier, 2005, pp. 31–107. doi:https://doi.org/10.1016/S0167-9244(05)80003-4.

[13] F. Yao, J. Zheng, M. Qi, W. Wang, Z. Qi, The thermal decomposition kinetics of poly(ether-ether-ketone) (peek) and its carbon fiber composite, Thermochimica Acta 183 (1991) 91–97. doi:https://doi.org/10.1016/0040-6031(91)80448-R.

[14] P. Patel, T. R. Hull, R. E. Lyon, S. I. Stoliarov, R. N. Walters, S. Crowley, N. Safronava, Investigation of the thermal decomposition and flammability of peek and its carbon and glass-fibre composites, Polymer Degradation and Stability 96 (1) (2011) 12–22. doi:https://doi.org/10.1016/j.polymdegradstab.2010.11.009.

[15] G. F. Levchik, K. Si, S. V. Levchik, G. Camino, C. A. Wilkie, The correlation between cross-linking and thermal stability: Cross-linked polystyrenes and polymethacrylates, Polymer Degradation and Stability 65 (3) (1999) 395–403. doi:https://doi.org/10.1016/S0141-3910(99)00028-2.

[16] M. Day, D. Budgell, Kinetics of the thermal degradation of poly(phenylene sulfide), Thermochimica Acta 203 (1992) 465–474. doi:https://doi.org/10.1016/0040-6031(92)85217-J.

[17] M. Starink, The determination of activation energy from linear heating rate experiments: a comparison of the accuracy of isoconversion methods, Thermochimica Acta 404 (1) (2003) 163–176. doi:https://doi.org/10.1016/S0040-6031(03)00144-8.

[18] W. Endres, M. D. Lechner, R. Steinberger, The kinetics of the thermal decomposition of thermoplastic polyurethane elastomers under thermoplastic processing conditions, Macromolecular Materials and Engineering 288 (6) (2003) 525 – 530, cited by: 18. doi:10.1002/mame.200390050.

[19] S. Vyazovkin, C. A. Wight, Model-free and model-fitting approaches to kinetic analysis of isothermal and nonisothermal data, Thermochimica Acta 340-341 (1999) 53–68. doi:https://doi.org/10.1016/S0040-6031(99)00253-1.

[20] P. Budrugeac, The evaluation of the non-isothermal kinetic parameters of the thermal and thermo-oxidative degradation of polymers and polymeric materials: its use and abuse, Polymer Degradation and Stability 71 (1) (2000) 185–187. doi:https://doi.org/10.1016/S0141-3910(00)00148-8.

[21] Y. Carpier, B. Vieille, F. Barbe, A. Coppalle, Meso-structure-based thermomechanical modelling of thermoplastic-based laminates subjected to combined mechanical loading and severe thermal gradients, Composites Part A: Applied Science and Manufacturing 162 (2022) 107165. doi:https://doi.org/10.1016/j.compositesa.2022.107165.

[22] A. Mouritz, A. G. Gibson, Fire Properties of Polymer Composite Materials, Vol. 143 of Solid Mechanics and Its Applications, Springer, 2006. doi:https://doi.org/10.1007/978-1-4020-5356-6.

[23] B. Vieille, A. Coppalle, C. Keller, M.-R. Garda, Q. Viel, E. Dargent, Correlation between post fire behavior and microstructure degradation of aeronautical polymer composites, Materials & Design 74 (2015) 76–85. doi:https://doi.org/10.1016/j.matdes.2015.03.002.

[24] A. Needleman, V. Tvergaard, An analysis of ductile rupture in notched bars, Journal of the Mechanics and Physics of Solids 32 (6) (1984) 461–490. doi:https://doi.org/10.1016/0022-5096(84)90031-0.

[25] E. Schuhler, Dégradation des matériaux composites sous l'effet d'une flamme : application à la réaction aux feux des composites utilisés pour les transports et l'énergie, Ph.D. thesis, thèse de doctorat dirigée par Coppalle, Alexis et Yon, Jérôme Energétique Normandie 2019 (2019).

[26] E. Schuhler, A. Chaudhary, B. Vieille, A. Coppalle, Fire behaviour of composite materials using kerosene burner tests at small-scales, Fire Safety Journal 121 (2021) 103290.

[27] N. Grange, Étude du comportement au feu de matériaux composites destinés à des applications aéronautiques : expériences et modélisations, Ph.D. thesis, INSA Centre Val de Loire, thèse de doctorat dirigée par Chetehouna, Khaled et Gascoin, Nicolas Energétique Bourges, INSA Centre Val de Loire 2018 (2018).

[28] M. Sherburn, Geometric and mechanical modelling of textiles (2007).

[29] Z-set software. http://www.zset-software.com/
[30] E. Rutherford, F. Soddy, Xli. the cause and nature of radioactivity part i and ii, The London, Edinburgh, and Dublin Philosophical Magazine and Journal of Science 4 (21) (1902) 370–396.
[31] J. Flynn, L. Wall, General treatment of the thermogravimetry of polymers, J Res Natl Bur Stand - Phys Chem 70A (1966) 487–523.
[32] Faa regulations. https://www.faa.gov/regulations_policies/faa_regulations

List of Figures

List of Tables